2021

Sea Surface Current Mapping with HF Radar – a Primer

Clifford R. Merz
University of South Florida, cmerz@usf.edu

Yonggang Liu
University of South Florida, yliu@usf.edu

Robert H. Weisberg
University of South Florida, weisberg@usf.edu

Chapter 4

Sea surface current mapping with HF radar – A Primer

Clifford R. Merz[1*], Yonggang Liu[1], Robert H. Weisberg[1]

[1]University of South Florida, College of Marine Science, 830 First Street South, St. Petersburg, FL 33701

*Corresponding author contact: cmerz@usf.edu

Shore-based oceanographic High Frequency (HF) radars are frequently used to remotely sense and map coastal sea surface currents. This chapter begins with a review of the development and utilization of HF radar sea-echo interactions and their relationship in the determination of the radial component of the sea surface current and vector coverage map, followed by a brief discussion of recent ongoing HF radar observations on the West Florida Shelf (WFS). Reported are HF radar performance and its complicated relationships with environmental factors.

1. Introduction

Ocean currents are the continuous movement of seawater. In the coastal ocean, the currents are what deliver nutrients from the deep-ocean and the estuaries to the shelf, thereby fueling primary productivity and initiating the complex biological and chemical interactions resulting in the shelf ecology [1]. Commercial and recreational fisheries depend on this as do blooms of harmful algae [2]. Similarly, safe and efficient maritime commerce and missing boater search and rescue operations depend on our ability to specify currents, sea level, and sea state on the basis of the ocean and atmosphere interactions.

Two different methods of current measurement are commonly in use: Lagrangian and Eulerian. The Lagrangian method tracks the path followed by the moving fluid and consists of placing a floating object in the water and allowing it to drift away from its initial position. This method has progressed from early efforts using floating coconuts and drifter bottles, a timer and the known distance traveled, to highly advanced instruments equipped with internal position logging and near- and real-time satellite transmission [3], and satellite-tracked surface drifters [4]. In the Eulerian method, a monitoring instrument is placed at a fixed location and the speed and direction of the moving fluid are measured with respect to that fixed location. Trends can be determined by analysis of the time series generated at that given point. Some examples of Eulerian measurements include: cable attached electro-mechanical current meters which measure the velocity at a single depth; bottom mounted upward looking and buoy mounted downward looking Acoustic Doppler Current Profilers (ADCP) which measure the velocity throughout the water column [5]. These in situ current observations are made at a single point at a time, which are very limited in spatial coverage.

Archived with permission from *Ocean Remote Sensing Technologies: High frequency, marine and GNSS-based radar*, *Weimin Huang & Eric W. Gill*, published by The Institution of Engineering and Technology, *2021*.
DOI: 10.1049/SBRA537E

In contrast to those traditional single-point current measurements, shore-based HF radars can map surface currents with large spatial coverages. They have become an important component of coastal ocean observing systems [6]. HF radar measured currents have been found in many oceanographic applications [7-9] as well as for assimilation in numerical ocean circulation models [10-12] because of their ability to remotely sense and map surface currents over large horizontal extents and at high sample resolution. Radiated by a vertically polarized shore-based antenna, transmitted HF electromagnetic (EM) radio waves (3-30 MHz) interact with ocean waves, resulting in Doppler shifted echoes backscattered by sea-surface gravity waves possessing a wavelength equal to one-half of the transmitted EM radar wave wavelength [13, 14]. The Doppler effect (also referred to as Doppler shift) is the change in frequency of a propagating wave in relation to an observer moving relative to the wave source and is named for Austrian physicist Christian Doppler who first described the phenomenon in 1842. Radar and sonar are but two of many successful examples where direct application of the Doppler principle is applied to measure the relative speed of a moving target.

As discussed in Chapter 1 [15], HF radar EM waves can propagate via two operational modes: 1) ground wave; and 2) sky wave. Here we consider the effects associated with ground wave propagation only to map sea surface currents using the concept of Bragg scattering at near-grazing incidence [16-20]. This chapter is written to serve as both a fundamental chapter on HF radar surface current mapping estimation as well as a companion to Chapter 5 [21].

2. Theory behind radial and vector current derivation from HF radar Doppler spectrum

Barrick [22] reported that HF radar sea echoes were first observed on air-defense nets around the English Channel during World War II where the resulting "clutter" periodically imposed limitations to the detection of aircraft. Based on HF radar experimental observations at 13.5 MHz, Crombie [16] was the first to correctly deduce the physical mechanism producing sea scatter and identify the distinctive features of sea-echo Doppler spectra. Crombie observed that the echo Doppler spectrum contained two dominant peaks symmetrically located about the transmitted EM radio carrier frequency.

Crombie reasoned that since there were two dominant peaks in the Doppler echo, the source of the originating scatter must be from two targets moving at a given velocity and that these "targets" were ocean wave trains with radial wave phase velocity components along the radar look direction. He further calculated the wavelength of the ocean wave train seen by the HF radar using the deep water gravity-wave dispersion relationship. Finally upon equating these two relationships, the wavelength of the backscattering ocean wave train, λ_{Ocean}, was found to equal one-half of the transmitted EM radar frequency wavelength, λ_{EM}.

The "resonant" effect often mentioned during HF radar operational discussions shares similar characteristics with Bragg backscatter, the same backscatter diffraction-grating mechanism associated with Braggs' law, which is widely applied to X-ray crystallography and laser holography [23, 24]. The λ_{Ocean} backscattered signal is in phase with the backscattered signal from

Archived with permission from *Ocean Remote Sensing Technologies: High frequency, marine and GNSS-based radar*, *Weimin Huang & Eric W. Gill*, published by The Institution of Engineering and Technology, *2021*.
DOI: 10.1049/SBRA537E

the next λ_{Ocean} wave of the wave train. With the result being an "amplified" signal strength when all the in-phase backscattered signals that reach the shore base receiver are summed together [25].

An important property of the HF sea echo is its random Gaussian nature. Since the heights of the Bragg-scattering waves are random variables, the sea echo must also be a random variable [26]. Through constructive interference of these backscattered EM waves, an energy peak can be detected in the HF radar spectra, from which the ocean variance density spectrum can be determined (Figure 4.1). The 1st order spectral maxima region (observed peak) is dependent solely on the Bragg resonant scattering effect and the surrounding 2nd order spectral return regions are caused by double scattering or non-linearities in the wave field [27, 28]. Barrick and Peake [29] and Barrick [23, 30] showed that to first and second order, the *average* sea-echo Doppler spectrum is related to the *average* sea wave height directional spectrum evaluated at the required first- and second-order Bragg wavenumbers [26]. While examining a sinusoidal sea wave-train, Wait [31] related the strength of the signal voltage at the Doppler-echo peak to the height of the Bragg-resonant wave train. Even though over 65 years have passed since these transformational contributions occurred, it's important to not let the many technical advances that have occurred since reduce these observation-based achievements to a mere footnote or passing reference and it is for this reason that the historical and albeit time-dated Figure 4.1 is included herein.

Although all of the sea wave trains on the sea surface interact with the transmitted EM radar wave, as noted above, the waves that can produce strong backscatter energy toward the radar are those that have wavelengths equal to half wavelengths of the EM waves, $\lambda_{Ocean} = \lambda_{EM}/2$, and are moving either toward (resulting in a positive Doppler shift in frequency [+ peak]) or away from the radar (resulting in a negative Doppler shift in frequency [- peak]). In the absence of any sea surface current, the Doppler positions of these peaks are proportional to the phase velocity of these waves. In the presence of any underlying radial component of the surface current at the point of scatter, the received signal frequency will be Doppler shifted from the transmitted frequency in accordance with the velocity of the sea surface current field within which the moving ocean wave is propagating [18, 19, 32].

The backscattered Doppler shift of the Bragg peak from the carrier frequency due to Bragg resonant scattering along a non-moving sea surface is given by the expression:

$$f_{BP} = \pm \sqrt{\left(\frac{gf}{\pi Co}\right)} \qquad (1)$$

where g is the acceleration due to gravity (9.8 m/s^2), f is the transmitted EM radar carrier frequency, and c_o is the vacuum speed of light (3.0 x 10^8 m/s) [33]. In the presence of non-zero sea surface current, both Bragg peaks are shifted in the same direction by a frequency amount Δ given by

$$\Delta = 2V_r f/c_o \qquad (2)$$

where V_r is the radial speed of the sea surface current along the look direction of the radar. By measuring Δ, the radial component (V_r) of the sea surface current can be calculated [34].

Archived with permission from *Ocean Remote Sensing Technologies: High frequency, marine and GNSS-based radar*, *Weimin Huang & Eric W. Gill*, published by The Institution of Engineering and Technology, *2021*.
DOI: 10.1049/SBRA537E

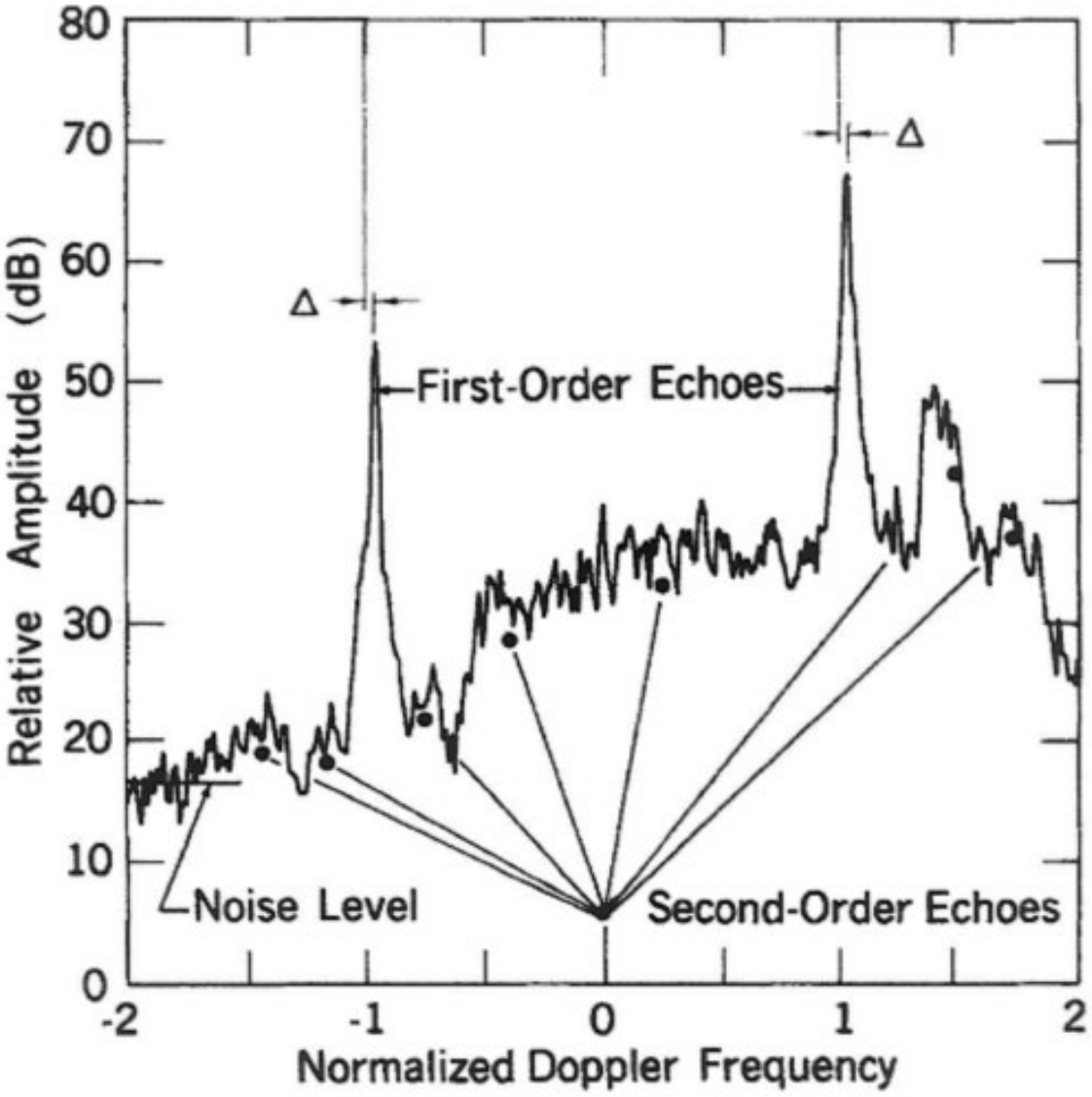

Figure 4.1. Example surface-wave sea-echo Dopler spectrum from a 13.4 MHz radar (Reprinted by permission from Springer Nature, Boundary-Layer Meteorology, HF Radio Oceanography – A Review, Barrick, D.E., Copyright 1978). The Doppler frequency units of the abscissa are normalized such that 0 corresponds to the transmitted EM carrier frequency (λ_{EM}) position, and ±1 refers to the predicted positions of the first-order Bragg echo peaks. Δ is the normalized frequency shift of the record due to the presence of a moving sea-surface current [22, 26].

A single HF radar only measures the radial component of the sea surface current by analyzing the Doppler spectra of the received backscattered signal. When two or more spatially separated HF radar sites are used, the calculation of a two-dimensional current vector surface coverage map can be made. In order for this to happen, the two sites must be adequately spaced and must overlook the same area of ocean from two different angles. The geometry for vectorization of the radial components of the sea surface current velocities measured by a two-site (master/slave) HF radar system in the overlap scattering area is shown in Figure 4.2 [35].

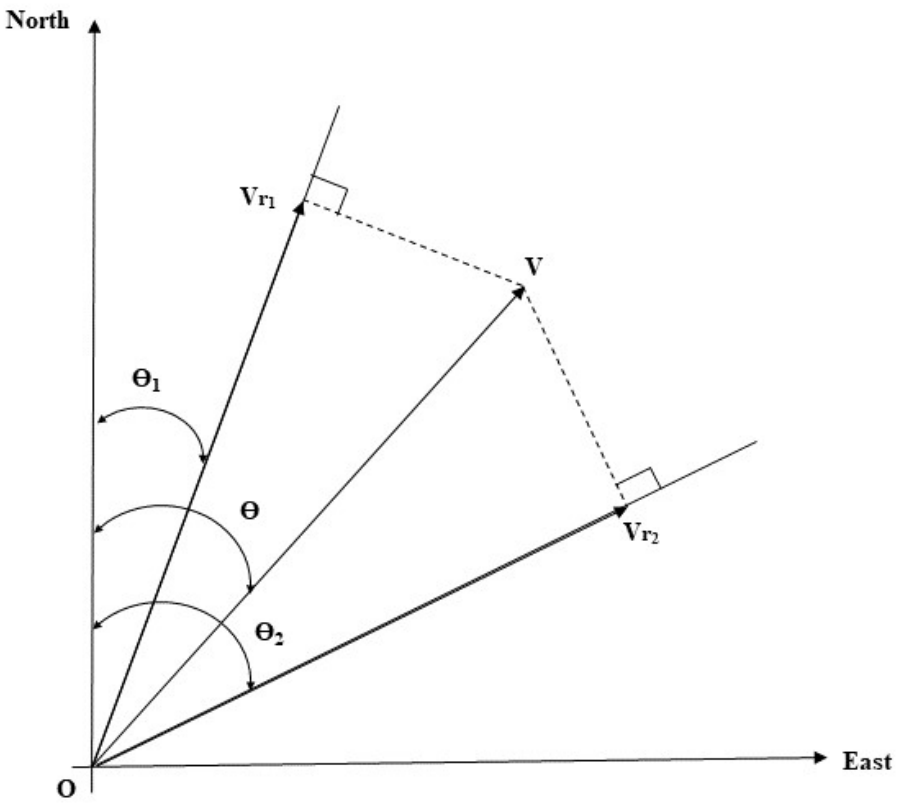

Figure 4.2. Cartesian geometry for vectorization of the radial components of the sea surface current velocities measured by a two-site HF radar system. Location O is the observed offshore sea surface within the overlap area. Source: Adapted from [35].

The vector current in the HF radar overlap observation area can be calculated from current radial components measured by two radars using the following expressions [33, 35]:

$$u = (V_{r1} \cos \Theta_2 - V_{r2} \cos \Theta_1) / \sin (\Theta_1 - \Theta_2) \quad (3)$$

$$v = (-V_{r1} \sin \Theta_2 + V_{r2} \sin \Theta_1) / \sin (\Theta_1 - \Theta_2) \quad (4)$$

where u and v are the eastward (or across-shelf) component and northward (or along-shelf) component of current, V_{r1} and V_{r2} are the radial components of the current vector measured by radars 1 (master) and 2 (slave), and Θ_1 and Θ_2 are referenced clockwise from the north are the beam directions for HF radars 1 and 2, respectively. The vector current shown in Figure 4.2 is $\mathbf{V} = u + i\,v$. Due to the different values of observation direction and range, radars located at different

site locations can have different backscattered echo intensities for the same portion of observed sea surface scattering area.

3. Factors Affecting Current Measurements

HF radar system current measurements depend upon many factors including the type of HF radar system used affecting radial current azimuthal resolution, range resolution, geometrical dilution of precision, signal propagation and sea state.

3.1 HF Radar System Types

Currently, two types of oceanographic HF radars are in frequent use worldwide: direction-finding HF radars such as the commercially available Seasonde developed by CODAR Ocean Sensors, Ltd, and phased array HF radars, such as the commercially available WERA developed by the University of Hamburg and manufactured by Helzel Messtechnik GmbH (Helzel). Other HF radar systems comprising these two types found in the technical literature include: COSRAD (James Cook University), LERA (University of Hawaii at Manoa), and OSMAR (Wuhan University, China).

The CODAR Seasonde direction-finding HF radar utilizes a compact directional receive antenna consisting of three collocated antenna elements (two orthogonally mounted loops and a vertical dipole or monopole element) in a single antenna housing. A single, omnidirectional antenna is used to transmit a pulsed, gated frequency modulated continuous wave (FMCW) waveform. The WERA phased array HF radar utilizes two separate, simultaneously operated antenna arrays: one for receiving and the other for transmitting FMCW chirps. WERAs utilize a 1-4 element array to transmit and a 12-16 element linear array to receive and record the backscattered radio wave signals. By virtue of the increased number of antennas, it can operate both in a direction-finding and directional beam-forming mode.

All HF radars resolve the target range and radial current speed to a high degree, however, system limitations exist in the ability to accurately determine the bearing of the specific surface scattering point. The Bragg region is taken to be a region of spread around the Bragg peaks whose energy and position are caused by Bragg-resonant waves and the underlying current velocity. Although the external factors affecting the strength of the received Bragg backscattered sea-echo signal may be the same, the mechanics of the reception and signal processing is different depending upon the HF radar system type used – phased array or direction-finding.

Phased array HF radars (such as the WERA) use multiple receive antennas and resolve signal arrival bearings using beamforming techniques. After fast Fourier transformation of the received signal, the time delays between antenna elements become phase shifts. The weighted signals at all the elements are summed in software to sweep a narrow beam across a series of desired azimuthal directions in which signals from particular arrival directions sum constructively, whereas signals for other arrival directions sum destructively, ultimately forming a steered beam across the radar footprint [34, 36, and 37]. On the other hand, in direction-finding HF radars (such as the CODAR SeaSonde), signal arrival bearings are resolved in software by fitting the data from

Archived with permission from *Ocean Remote Sensing Technologies: High frequency, marine and GNSS-based radar*, *Weimin Huang & Eric W. Gill*, published by The Institution of Engineering and Technology, *2021*.
DOI: 10.1049/SBRA537E

all 3 elements of the compact receive antenna to either a measured or modeled antenna response function consisting of relative phase and amplitude versus bearing with the direction of arrival (DOA) determined using the Multiple Signal Classification (MUSIC) algorithm [38-41]. The Doppler shift (or radial current velocity) is calculated for each frequency bin in the region followed by a determination of the ultimate DOA for that radial current velocity [42]. While MUSIC has advantages, attention must be paid during operational times of low signal-to-noise ratio (SNR) (the general SNR cut-off threshold is 6 dB) and if variations occur in the measured receive antenna beam pattern in order to minimize observational errors [43].

In both system types, the antenna pattern distortion and DOA algorithms will affect the azimuth accuracy and resolution of current radial component and vector accuracies. It should also be noted that the coherent integration (or dwell) time used for Fourier transformation will affect the Doppler resolution of the spectrum and, thus, the current speed accuracy.

3.2 Range Resolution

As discussed in Chapter 1 [15], range resolution is an important parameter affecting spatial resolution of HF radar current measurements. The relationship between FMCW bandwidth and range cell resolution (cell depth) for some typical settings is presented in Table 4.1 [44].

Table 4.1. Relationship between bandwidth and range cell resolution (depth) for a FMCW chirp.

Bandwidth (kHz)	Range Resolution (km)
25	**6.0**
50	**3.0**
100	**1.5**
150	**1.0**
250	**0.6**

The maximum bandwidth available, and therefore the range resolution used, is usually set by the local or regional frequency licensing authority, for example the Federal Communications Commission (FCC) in the United States of America.

3.3 Geometrical Dilution of Precision

The HF radar site-to site separation distance and transmit frequency control the size and shape of the domain where currents can be resolved through the geometry of the intersection angles of the radial component of the sea surface currents. This influence of the geometry on the surface current measurement errors is known as the Geometrical Dilution of Precision (GDOP). GDOP describes the reduction of accuracy caused solely by geometry and does not take into account the effects of reduced SNR that might be expected to decrease the accuracy of the current estimates in the farthest range bins [45].

Chapman *et al*. [45] derived the GDOP for the Cartesian current components based on the radar's mean look direction and the half angle between the intersecting beams. The GDOP is defined as

Archived with permission from *Ocean Remote Sensing Technologies: High frequency, marine and GNSS-based radar*, *Weimin Huang & Eric W. Gill*, published by The Institution of Engineering and Technology, *2021*.
DOI: 10.1049/SBRA537E

the variance ratio of (σ_u/σ) and (σ_v/σ) where σ is the total root mean square (RMS) variance of current differences [34]. When the azimuthal difference between the two HF radar beams is a right angle (90°), the current vector measurement error is at its minimum value. When the azimuthal difference becomes very different from a right angle, the aspect ratio of the contour changes from unity and the measurement error increases [35] with major variations occurring within the radar's near and far fields. For each grid point the X- and Y- components of GDOP are calculated depending upon the angular positions relative to each other, with radial velocity data from GDOP regions that exceed specified input criteria excluded from vector current estimation.

3.4 Signal Propagation and Sea State

For a given radar system, the broadness of the Doppler spectrum and the noise level are dependent on the sea state [46]. Regardless of the HF radar system used, successful current measurement depends upon the quality and magnitude of the received signal relative to noise level. The extent of the offshore working range is ultimately determined by the SNR, which in turn depends upon the sea surface roughness (or sea state), the radar's operating frequency and corresponding propagation loss, and the background noise level at the receive antenna.

Depending upon the frequency, EM waves can be affected by parameters relevant to both the sea and the atmosphere; two such possible sources include:

1) Variations in the viscosity and complex relative dielectric constant (ϵ) of the seawater. The attenuation of HF propagation is dependent on the imaginary part of ϵ, frequency and conductivity, where the conductivity is a function of the salinity and temperature [37, 47].
2) The atmospheric radio refractivity (N), which is dependent upon variations in the atmospheric humidity, temperature, and air pressure [48, 49]. However, it is well-known these effects are considered minimal within the HF frequency band.

The backscattered signal can be strongly affected by the sea state. A well-defined statistic to denote the characteristic height of the random waves in a sea state is the significant wave height (H_s), defined as the mean wave height, trough to crest, of the highest 1/3 of the waves measured.

As reported by Maresca *et al*. [50], for high sea states, the backscattered power is larger than for smaller sea states. Liu *et al.* [51] reported that the radial offshore coverage on the WFS decreased rapidly once H_s dropped below 1 m and decreased to about 60% of its peak value when H_s decreased to 0.5 m. However, the HF radar data quality remained satisfactory until H_s decreased below 0.3m corresponding to a RMS wind speed of <3 m/s.

4. HF Radar Current Observations on the West Florida Shelf

The University of South Florida (USF) Coastal Ocean Monitoring and Prediction System (COMPS) HF radar network consists of six operational sites: four long-range CODAR Seasonde direction-finding systems operating at 4.9 MHz and two 12-element WERA phased array systems operating between 12.275 and 13.20 MHz, all overlooking an array of moored instrumentation (surface meteorology and water column ADCP velocity, temperature and salinity), which together

Archived with permission from *Ocean Remote Sensing Technologies: High frequency, marine and GNSS-based radar*, *Weimin Huang & Eric W. Gill*, published by The Institution of Engineering and Technology, *2021*.
DOI: 10.1049/SBRA537E

comprise a unique HF radar testbed along the WFS and lower Florida Keys region. The combined HF radar network provides real-time sea surface current measurements on the WFS with footprints of the network coverage shown in Figure 4.3. Detailed operational specifications and performance measurements covering these specific sites along with detailed discussion of the combined USF HF radar network, overall system layout, remote site design, and general COMPS program can be found in [52 – 55]. The CODAR radial current velocity (radials) and vector totals are processed using standard CODAR software with a nominal range and bearing of 5.8 km and 5°, respectively and a transmit bandwidth of 25.734 kHz. WERA radial current velocity (radials) and vector totals are processed using standard WERA software with a nominal range and bearing of 1.5 km and 10°, respectively, but at broadside (90°) changing to 1.5 km and 20° at +/- 60°. The WERA systems provide the ability to set the measurement bandwidth or utilize an adaptive noise reduction algorithim to dynamically adapt the HF radar center transmit frequency and measurement bandwidth to locally varying Radio Frequency Interference (RFI) conditions.

As previously mentioned, a single radar site can only measure the radial velocity component of the sea surface current. Thus, radial currents from two or more sites are required to calculate two-dimensional vector surface currents. Figure 4.4 presents an example of a measured sea surface radial component velocity field from the USF COMPS CODAR Venice HF radar site. Figures 4.5 and 4.6 show typical measured sea surface vector current field maps using radial velocities from USF COMPS CODAR and WERA HF radar sites, respectivily.

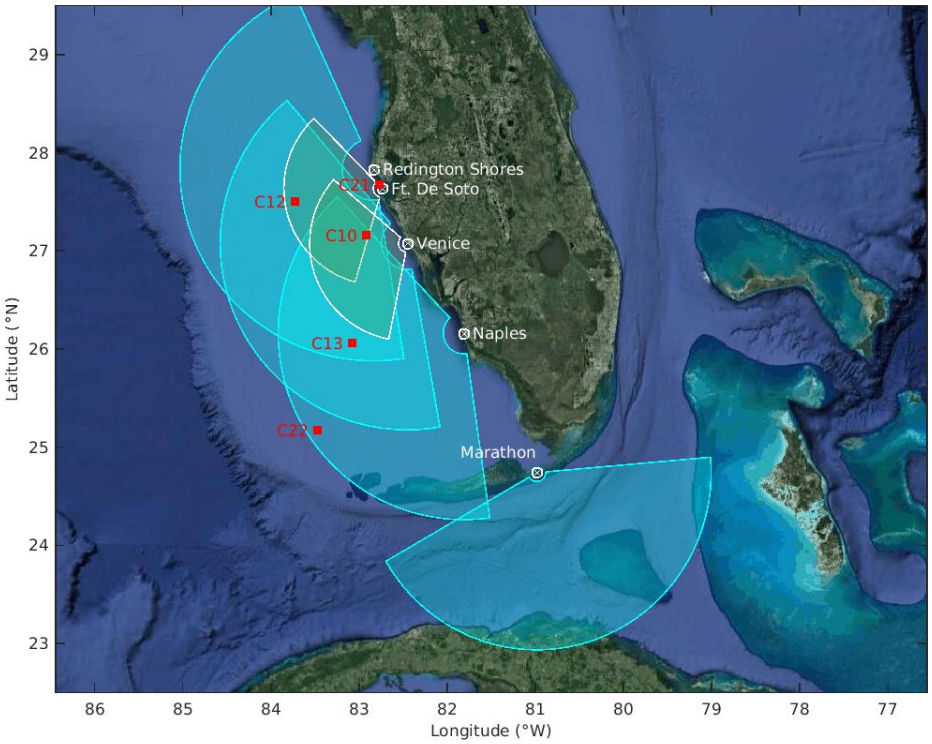

Figure 4.3. Theoretical coverages of the USF COMPS HF radars on the WFS (Redington Shores, Ft. De Soto, Venice, and Naples, Florida) and in the Florida Keys (Marathon, Florida) overlooking the Straits of Florida. Also shown are the locations of the real- time moorings (C10, C12, C13, C21 and C22) on the WFS.

Archived with permission from *Ocean Remote Sensing Technologies: High frequency, marine and GNSS-based radar*, *Weimin Huang & Eric W. Gill*, published by The Institution of Engineering and Technology, *2021*.
DOI: 10.1049/SBRA537E

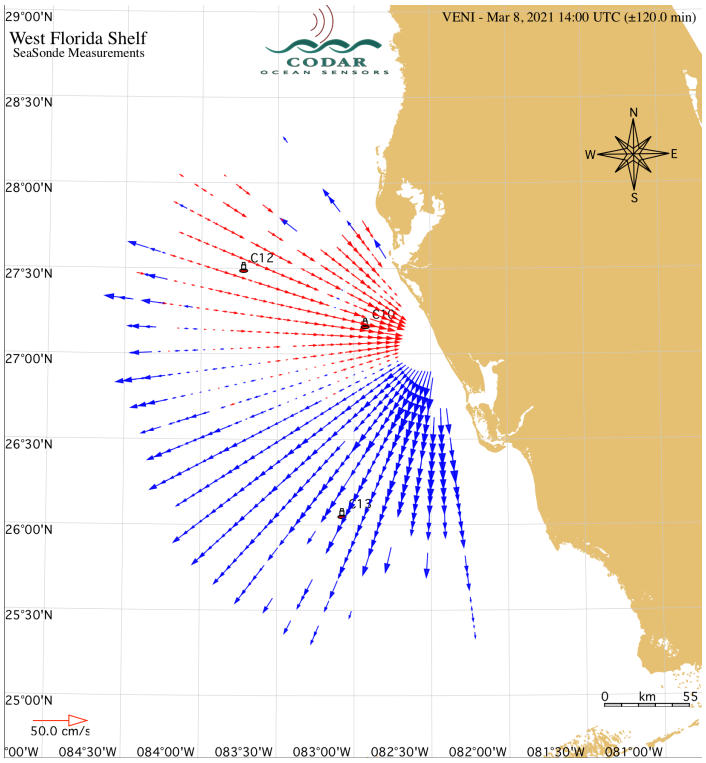

Figure 4.4. Example of measured CODAR sea surface radial component velocity field from the USF COMPS Venice Site. Dual colors signify radial vectors coming either toward the radar (red) or moving away (blue).

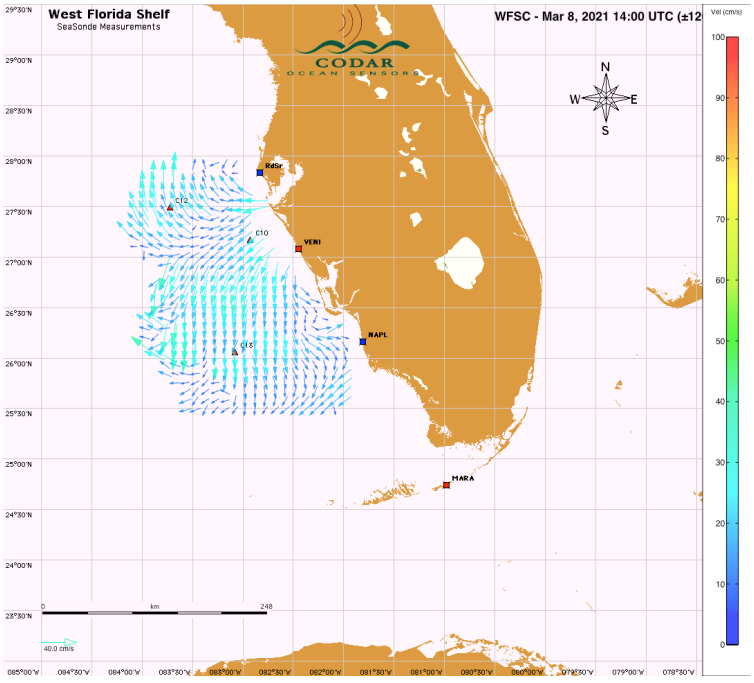

Figure 4.5. Example of measured CODAR sea surface current field using radial velocities from the USF COMPS WFS Redington Shores, Venice, and Naples HF radar sites.

Archived with permission from *Ocean Remote Sensing Technologies: High frequency, marine and GNSS-based radar*, *Weimin Huang & Eric W. Gill*, published by The Institution of Engineering and Technology, *2021*.
DOI: 10.1049/SBRA537E

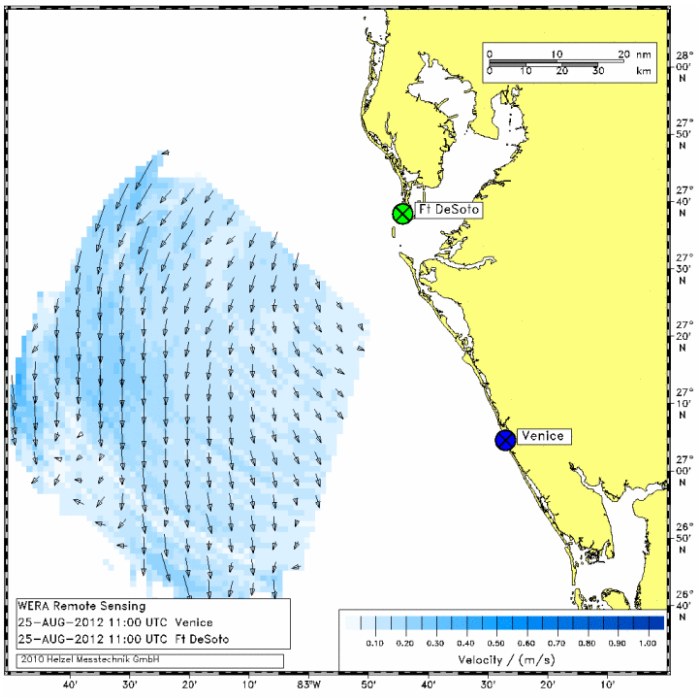

Figure 4.6. Example of measured WERA sea surface current field using radial velocities from the USF COMPS WFS Ft De Soto and Venice HF radar sites.

Hourly data from each remote HF radar site are pulled via scripting to a central processing station located at the USF College of Marine Science in St Petersburg, Florida, where the data are processed and web served in near real-time through the COMPS Website http://comps.marine.usf.edu, the Southeast Coastal Ocean Regional Association (SECOORA) Website http://secoora.org, and the U.S. Integrated Ocean Observing System (IOOS) National HF Radar Network's Coastal Observing Research and Development Center (CORDC) Website http://cordc.ucsd.edu/projects/mapping/stats, where they are ultimately integrated into ocean models for various uses such as improved boater safety, supporting U.S Coast Guard Search and Rescue (SAR) operations, and oil spill tracking within the Gulf of Mexico. An evaluation of observed radial surface currents in the Straits of Florida using the Marathon HRF site data is provided in Chapter 5.

5. Ongoing HF Radar Investigations on the West Florida Shelf

CORDC provides useful individual HFR site diagnostic pages with specific performance parameters and time series for near real-time monitoring. One particularly useful operational parameter is the offshore working range and the observance of periodic variations. One possible cause of these offshore range variations is the low sea state conditions typically found on the WFS during various times of the year which can result in low backscatter. Reduced backscatter does not necessarily produce higher current measurement errors, but it reduces the SNR and corresponding offshore working range. The SNR can be reduced further by increases of the ambient background noise through changes in the local electromagnetic RFI environment (i.e.,

Archived with permission from *Ocean Remote Sensing Technologies: High frequency, marine and GNSS-based radar*, *Weimin Huang & Eric W. Gill*, published by The Institution of Engineering and Technology, *2021*.
DOI: 10.1049/SBRA537E

diurnal ionospheric variations, weather-related lightning, local radio stations, near-shore manufacturing centers, airports, and ship traffic) [46].

5.1 An Event of Offshore Working Range Drop

Observance of the CORDC offshore working range time series data during the November/December 2020 time period revealed, to varying degrees, a several-day range level drop at all 5 WFS HF radar sites. According to a previous study on HF radar data returns on the WFS, the 4.9 MHz CODAR system's data return was closely related with the conditions of sea state, while the ~12.7 MHz WERA system's performance did not exhibit an obvious sea state relationship [55]. Thus, we focus herein on the WERA system for the remainder of this chapter. This low data return event is analyzed using the coastal ocean observations available during those days. Real-time data from the Ft. De Soto HF radar and C12 air-sea interaction buoy were selected for discussion because of their relative proximity and the C12's near-broadside location within the Ft De Soto HF radar offshore coverage area (Figure 4.3).

Figure 4.7 presents the 31-day (November 11 – December 11, 2020 offshore working range real-time data measured by the Ft. De Soto WERA HF radar operating between 13.1 and 13.2 MHz. A drop in offshore range is observed during the 4-day (November 26 – 29, 2020) time period.

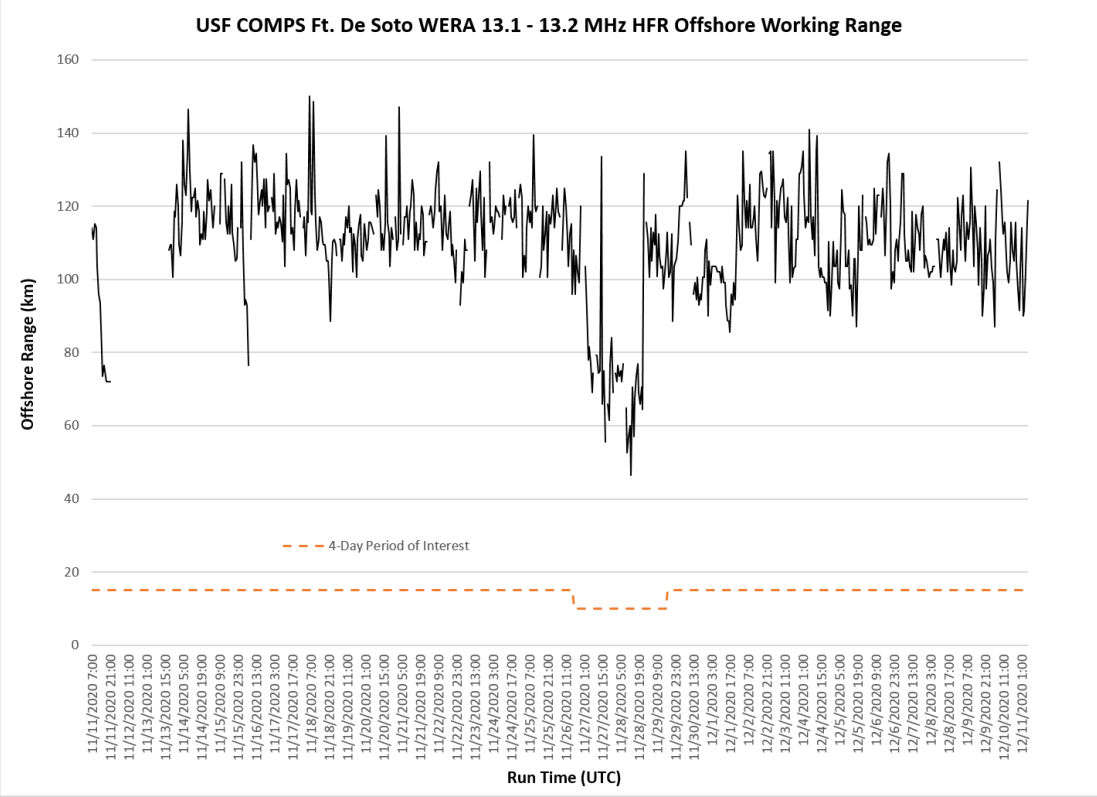

Figure 4.7. USF COMPS Ft De Soto WERA HF radar offshore working range covering the 31-day period between November 11 to December 11, 2020. Real-time data downloaded from CORDC's FDS site diagnostic page. Highlighted 4-day period of interest covers November 26 to 29, 2020.

Archived with permission from *Ocean Remote Sensing Technologies: High frequency, marine and GNSS-based radar*, *Weimin Huang & Eric W. Gill*, published by The Institution of Engineering and Technology, *2021*.
DOI: 10.1049/SBRA537E

As mentioned, the extent of the offshore working range is ultimately determined by the SNR, which, in turn, depends upon several environmental variables including the background noise level at the receive antenna, the radar's operating frequency and corresponding propagation loss, and sea surface roughness. Investigations into several of these variables were conducted and are presented herein while other variables are currently under examination.

5.2 Average Background Noise and RFI Effect

Both of the COMPS WFS WERA HF radar systems utilize the "Listen-Before-Talk" (LBT) adaptive noise reduction algorithm to dynamically adapt the HF radar center transmit frequency and measurement bandwidth to varying local RFI conditions. Performing like a spectrum analyzer using 32 linear frequency chirps with the transmitter turned off, prior to each full acqusition a 1-minute pre-scan measurement is made across the entire anticipated frequency band. Real-time analysis of the pre-scan data reveals regions of varying external noise with the quietest allowable bandwidth determined and the corresponding mid span transmit frequency selected for subsequent use in the following full measurement. If the frequency pre-scan detects too much external noise, the measurement bandwidth is reduced, which, in turn, increases the individual range cell size [44, 56, and 57] as shown in Table 4.1.

Storage and plotting of the pre-scan values allow for the generation of a time-series of 1-minute "snapshots" of the average noise power level calculated across approximately the center frequency and bandwidth used in the actual follow-on measurements. The pre-scan measurement value contains background noise (e.g., atmospheric such as thunderstorms, local wide-band sources) and varying signals from other radio transmitters, including those very far away reflected by the ionosphere, which appear as RFI. Much of the RFI clutter present in the pre-scan is reduced/mitigated during subsequant WERA processing so it is not the actual value the WERA "sees" during later processing. However, examination at this stage is useful in looking at the variation and magnitude of the RFI present as compared to the characteristic shape and median value of the average sum of the background noise and RFI data.

Figure 4.8 presents the average sum of the background noise and RFI pre-scan data as measured by the Ft De Soto WERA HF radar system under the application of WERA's LBT adaptive algorithm during the 31-day period. The transmitted operational central frequency was between 13.1 and 13.2 MHz with bandwidths varying between 25 to 100 kHz. There is no significant change observed in the average background noise during the 4-day (November 26 – 29, 2020) period as opposed to the entire 30-day period. This indicates that the drop in offshore range is related to a reduction in backscattered signal and not a increase in local background noise.

The distance between the Venice and Ft. De Soto WERA sites shown in Figure 4.3 is ~68.5 km. As expected graphical results for the Venice WERA HF radar pre-scan data reveal similar results to that presented for Ft. De Soto in Figure 4.8, with many of the same RFI signals but differing slightly in strength due to the separation distance. Table 4.2 summarizes the background noise levels for both the Ft De Soto and Venice WERA HF radar sites.

Table 4.2. Pre-scan summary of the median value of the average sum of measured background noise and radio frequency interference

Days/Date	Ft DeSoto WERA	Venice WERA
31-day (Nov 11 – Dec 11, 2020)	-82.3 dB	-82.7 dB
4-day (Nov 26 – Nov 29, 2020)	-82.0 dB	-82.3 dB

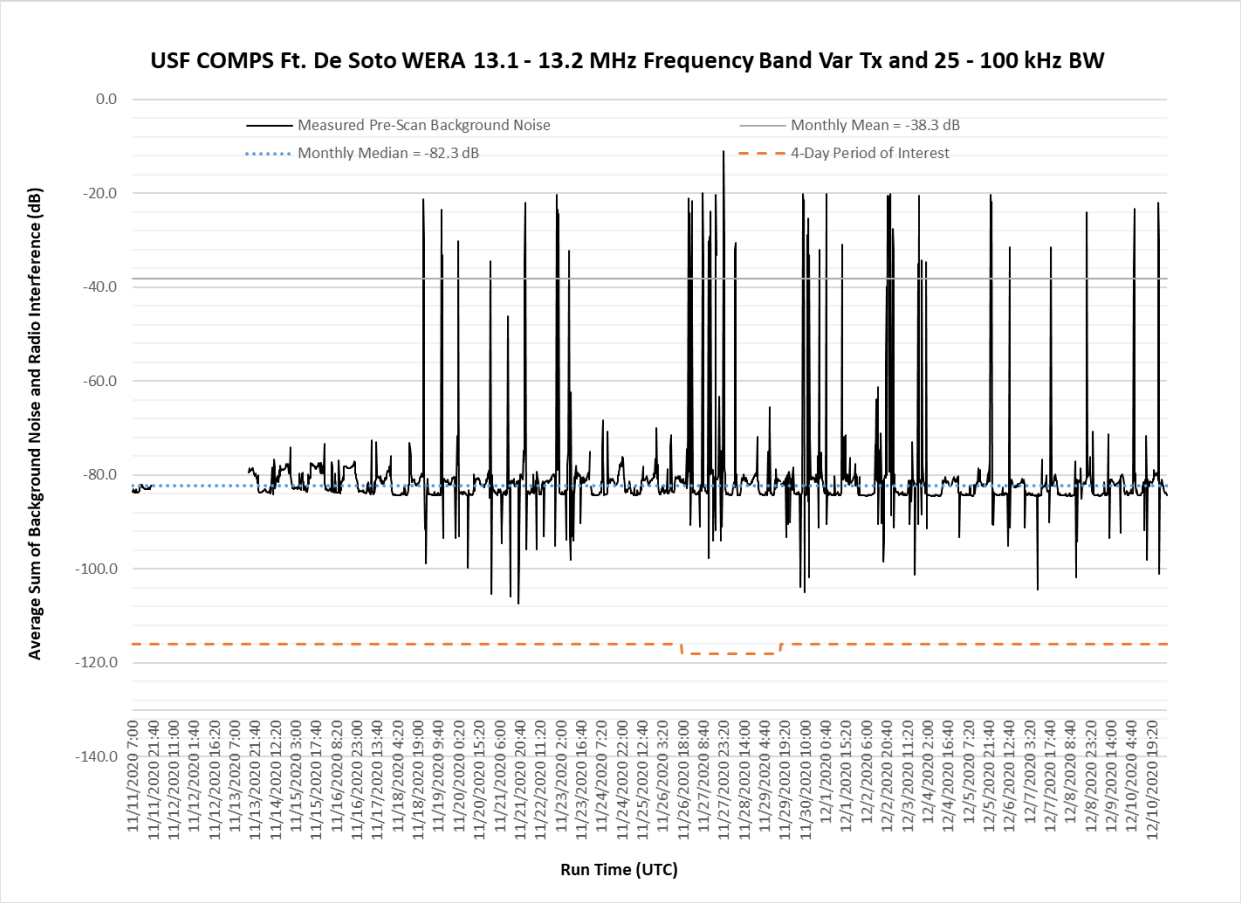

Figure 4.8. USF COMPS Ft De Soto WERA HF Radar average sum of background noise and radio interference during the 31-day period November 11 to December 11, 2020. Highlighted 4-day period of interest covers November 26 to 29, 2020.

5.3 Atmospheric Radio Refractivity (*N*) Effect

Figure 4.9 presents the computed Atmospheric Radio Refractivity [*N*] for the period November 11 through December 11, 2020 using data obtained from the COMPS C12 air/sea interaction buoy.

The value of ***N*** is computed according to the ITU-R [48] as:

$$N = \frac{77.6}{T}\left(P + 4810\frac{E}{T}\right) \qquad (5)$$

Archived with permission from *Ocean Remote Sensing Technologies: High frequency, marine and GNSS-based radar*, *Weimin Huang & Eric W. Gill*, published by The Institution of Engineering and Technology, *2021*.
DOI: 10.1049/SBRA537E

where P = atmospheric pressure (hPa), E = water vapor pressure (hPa), T = absolute temperature (K). The relationship between water vapor pressure (E) and relative humidity (H) is given by:

$$E = (H)(Es)/100 \quad (6)$$

$$Es = a \exp(bt/(t+c)) \quad (7)$$

where H = relative hunidity (%), t = temperature (°C), Es = saturation vapor pressure (hPa) at the temperature t (°C) and the coefficients a, b, c for water are:

a = 6.1121, b = 17.502, c = 240.97 (valid between -20° to +50° with a ±0.20% accuracy).

As expected, no significant change was observed in the Atmospheric Radio Refractivity values during November 26 – 29, 2020, thus, confirming and quantifying prior well-known expressed comments that the strength of the first-order echo returns is not dependent upon air temperature, relative humidity or barometric pressure within the HF frequency band.

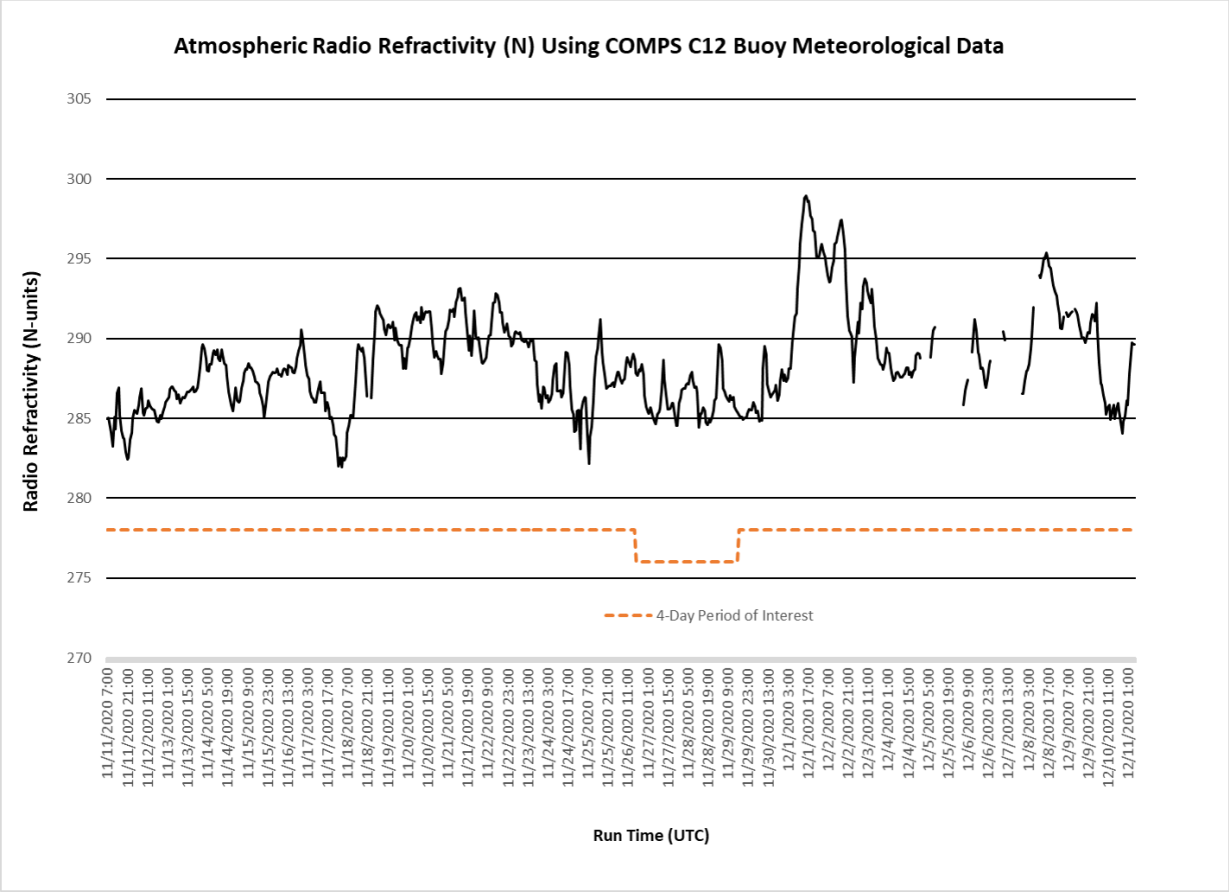

Figure 4.9. USF COMPS C12 Meteorological Buoy Computed Atmospheric Radio Refractivity covering the 31-day period November 11 to December 11, 2020. Highlighted 4-day period of interest covers November 26 to 29, 2020.

Archived with permission from *Ocean Remote Sensing Technologies: High frequency, marine and GNSS-based radar*, *Weimin Huang & Eric W. Gill*, published by The Institution of Engineering and Technology, *2021*.
DOI: 10.1049/SBRA537E

5.4 Wind Speed Effect

Figure 4.10 presents the wind speed for the same 31-day period using wind data converted to 10m height obtained from the COMPS C12 air/sea interaction buoy. There is a similiar drop in the wind speed during the same 4-day time period. Superimposed on Figure 4.10 is the computed wind speed RMS during the 4-day low wind (~3.4 m/s) event and the remaining 27 days (9.0 m/s). While the computed 4-day 3.4 m/s wind speed RMS compares favorably to the <3 m/s wind speed RMS previously observed on the WFS by Liu *et al*. [53] and briefly discussed in Section 3.4, close examination of Figure 4.10 reveals other periods in the record of equally low wind speed RMS values without a corresponding drop in the offshore working range of the Ft De Soto WERA HF radar (Figure 4.7).

Although a telling clue in itself, the wind speed is but a contributor to the underlying cause. Wave height is affected by wind speed, wind duration (or how long the wind blows), and fetch (the distance over water that the wind blows in a single direction). If the wind speed is low, only small waves appear, regardless of wind duration or fetch. Weakening winds may result in the reduction of the sea state and corresponding scattering strength of the rough sea surface which, in turn, increases the backscattered signal's propagation loss. Work is continuing on examining the interaction of energy loss and backscattering strength in terms of sea state and seawater physical conditions (e.g., water temperature and salinity) as they may relate to attenuation of the EM wave propagation along the sea surface.

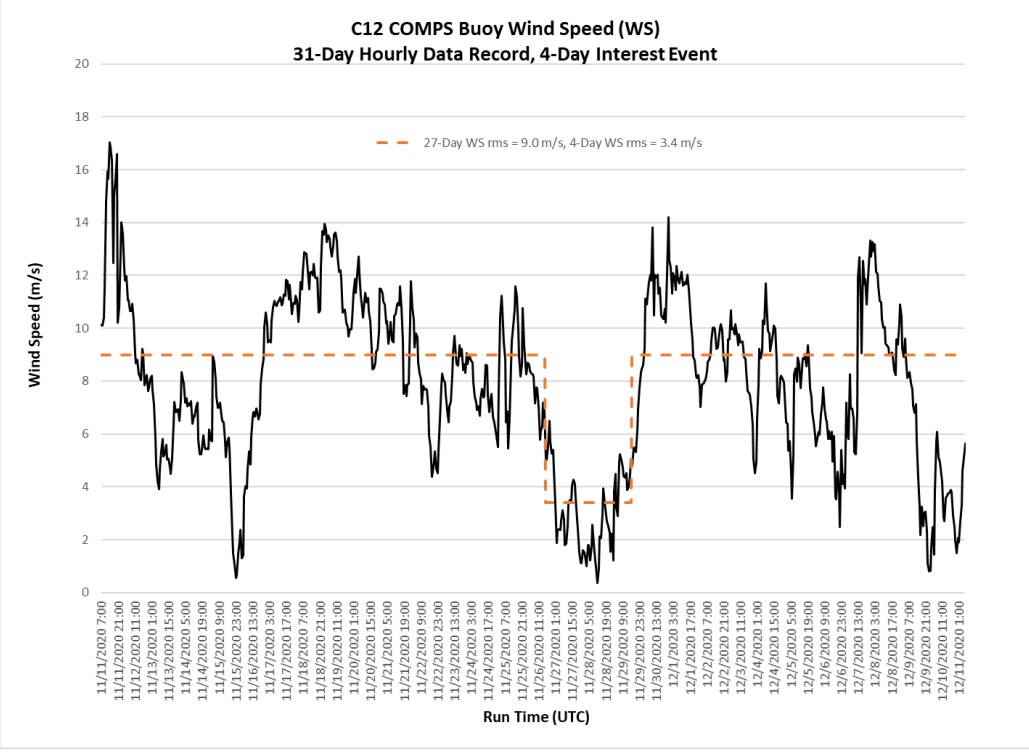

Figure 4.10. USF COMPS C12 meteorological buoy wind speed at 10m height covering the 31-day period November 11 to December 11, 2020. Highlighted 4-day period of interest covers November 26 to 29, 2020.

Archived with permission from *Ocean Remote Sensing Technologies: High frequency, marine and GNSS-based radar*, *Weimin Huang & Eric W. Gill*, published by The Institution of Engineering and Technology, *2021*.
DOI: 10.1049/SBRA537E

6. Summary

Sea surface current measurements using oceanographic HF radar systems are reviewed followed by a brief discussion of recent on-going HF radar observations on the WFS. Overall HF radar system performance of current measurement depends upon many external factors including: oceanic conditions, type of HF radar system used, SNR of the signal received at the shore based radar antennas, frequency resolution of the Doppler spectrum, and the accurate identification of the Bragg peaks. Challenges of HF radar current observation on the WFS are often manifested in low SNR, reduced data returns and offshore range. A careful review of these factors along with a thorough evaluation of the unique environmental characteristics surrounding the site location under consideration for use is required in order to achieve a successful measurement outcome.

Acknowledgements:

Support was provided by NOAA via the U.S. IOOS Office through the Southeast Coastal Ocean Observing Regional Association (SECOORA); NOAA Award Number NA16NOS0120028, SECOORA Sub Number: IOOS.16 (028) USF.BW.OBS-HFR.1. This work was supported by the Gulf Research Program of the National Academies of Sciences, Engineering, and Medicine under the Grant Agreement number: 2000009917. The content is solely the responsibility of the authors and does not necessarily represent the official views of the Gulf Research Program or the National Academies of Sciences, Engineering, and Medicine. This work was also supported by the University of South Florida's College of Marine Science via the Coastal Ocean Monitoring and Prediction System (COMPS) program. USF seagoing buoy activity is attributed to J. Law with J. Donovan providing real-time data management competency. USF HF Radar Network activity is attributed to C. Merz. We thank H. Parikh (CODAR Ocean Sensors, Ltd., CODAR), K-W Gurgel (Univ. of Hamburg, WERA), and L. Petersen (Helzel Messtechnik GmbH, WERA) for their technical discussions and suggestions and to L. Petersen (Helzel Messtechnik GmbH, WERA) for creating the custom script used to retrieve the pre-scan average noise level of the LBT selected band from a .RAW_ascii file and append it to a log file. We also thank J. Chen, M. Otero, and T. Cook (CORDC) for HF radar diagnostic page data downloads.

References:

[1] Weisberg R.H., Zheng L., Liu Y. 'Basic tenets for coastal ocean ecosystems monitoring: A West Florida perspective', in Coastal Ocean Observing Systems. 2015; 40-57, Elsevier (Academic Press), London, UK, http://dx.doi.org/10.1016/B978-0-12-802022-7.00004-3.

[2] Weisberg R.H., Liu Y., Lembke C., Hu C., Hubbard K., Garrett M. 'The coastal ocean circulation influence on the 2018 West Florida Shelf K. brevis red tide bloom'. *J. Geophys. Res. Oceans*, 2019; **124**:2501-2512, https://doi.org/10.1029/2018JC014887.

[3] Merz C.R., Weisberg R.H., Smith P., Law J., Cole R.D., Donovan J., *et al*. 'Development of a Self-Contained, Satellite Based, Surface Buoy Position Tracking Device'. *MTS/IEEE Oceans 2007 Conference Proceedings*. 2007, doi: 10.1109/OCEANS.2007.4449363.

[4] Liu Y., Weisberg R.H., Hu C., Kovach C., Riethmüller R.. 'Evolution of the Loop Current system during the Deepwater Horizon oil spill event as observed with drifters and satellites', in Monitoring and Modeling the Deepwater Horizon Oil Spill: A Record-Breaking Enterprise, *Geophys. Monogr. Ser*. 2011; **195**:91-101, doi: 10.1029/2011GM001127.

[5] Weisberg R.H., Liu Y., Mayer D.A. 'Mean circulation on the west Florida continental shelf observed with long-term moorings'. *Geophys. Res. Lett*. 2009: **36**, L19610, doi: 10.1029/2009GL040028.

[6] Liu Y., Kerkering H., Weisberg R.H. (eds.) *Coastal Ocean Observing Systems*, ISBN 978-0-12-802022-7, London: Academic Press. 2015. P.461.

[7] Abascal A.J., Castanedo S., Medina R., Losada I. J., Álvarez-Fanjul E. 'Application of HF radar currents to oil spill modelling'. *Marine Pollution Bulletin*. 2009; **58**:238–248, doi:10.1016/j.marpolbul.2008.09.020.

[8] Zelenke B.C., Moline M.A., Jones B.H., Ramp S.R., Crawford G.B., Largier J.L., et al. 'Evaluating connectivity between marine protected areas using CODAR high-frequency radar' *Proceeding at OCEANS MTS/IEEE, Biloxi, MS* 2009. doi:10.23919/OCEANS.2009.5422272; 2009.

[9] Roarty H., Glenn S., Kohut J., Gong D., Handel E., Rivera E., et al. 'Operation and Application of a Regional High-Frequency Radar Network in the Mid-Atlantic Bight'. *Marine Technology Society Journal.* 2010; **44**(6):133-145.

[10] Lewis J.K., Shulman I., Blumberg, A.F. 'Assimilation of CODAR observations into ocean models'. *Continental Shelf Research*. 1998; **18**:541-559.

[11] Paduan J.D., Shulman I. 'HF radar data assimilation in the Monterey Bay area'. *Journal of Geophysical Research*. 2004; **109**:C07S09, doi: 0.1029/2003JC001949.

[12] Barth A., Alvera-Azcárate A., Weisberg R.H. 'Assimilation of high-frequency radar currents in a nested model of the West Florida Shelf'. *Journal of Geophysical Research*. 2008; **113**:C08033, doi: 10.1029/2007JC004585.

[13] Barrick D.E., Evans M.W., Weber B.L. 'Ocean surface currents mapped by radar'. Science. 1977; **198**:138–144, doi:10.1126/science.198.4313.138.

[14] Lipa B.J., Nyden B. 'Directional Wave Information from the SeaSonde'. *IEEE Journal of Oceanic Engineering*. 2005; **30**(1): 221-231.

[15] Gill E.W., Huang W. 'HF Radar in a Marine Environment'. Chapter 1 in Gill E. & Huang W. (eds.) Ocean Remote Sensing Technologies: High Frequency, Marine and GNSS-Based Radar. IET. 2021.

[16] Crombie D.D. 'Doppler spectrum of sea echo at 13.56 Mc/s', *Nature.* 1955; **175**:681-682.

[17] Stewart R.H., Joy J.W. 'HF radio measurements of surface currents'. *Deep-sea Res.* 1974; **21**:1039-1049.

[18] Barrick D.E. 'Extraction of wave parameters from measured HF radar sea-echo Doppler spectra'. *Radio Sci.*, 1977a; **12**:415-424.

[19] Barrick D.E. 'The ocean wave height non-directional spectrum from inversion of the HF sea-echo Doppler spectrum'. *Remote Sens. Environ.* 1977b; **6**:201-227.

[20] Paduan J.D., Graber H.C. 'Introduction to high-frequency radar: Reality and myth'. *Oceanography.* 1997; **10**:36-39.

[21] Liu Y., Merz C.R., Weisberg R.H., Shay L.K., Glenn S., Smith M. 'An Initial evaluation of high-frequency radar radial currents in the Straits of Florida in comparison with altimetry and model products'. Chapter 5 in Gill E. & Huang W. (eds.) Ocean Remote Sensing Technologies: High Frequency, Marine and GNSS-Based Radar. IET. 2021.

[22] Barrick D.E. 'HF Radio Oceanography – A Review'. *Boundary-Layer Meteorology*. 1978; 13:23-43.

[23] Barrick D.E. 'First-Order Theory and Analysis of MF/HF/VHF Scatter from the sea'. *IEEE Transactions on Antennas and Propagation.* 1972a; AP-20:2-10.

[24] Wang W., Gill E. 'High-Resolution Spectral Estimation of HF Radar for Current Measurement Applications'. *Journal of Atmospheric and Oceanic Technology*. 2015; **32**(8):1515-1525, doi: 10.1175/JTECH-D-14-00191.1.

[25] High Frequency Radar (HF Radar). 1999. Rutgers University Institute of Marine and Coastal Sciences. Available from https:// web. archive. org/ web/ 20210309192121/https://marine.rutgers.edu/cool/education/class/josh/hf_radar.html [accessed 9 April 2021].

[26] Barrick D.E., Snider J.B. 'The Statistics of HF Sea-Echo Doppler Spectra'. *IEEE Transactions on Antennas and Propagation.* 1977; AP-25:19-28.

[27] Barros F.F.C. 'Validation and Quality Assessment of HF Radar Wave Measurements in the Algarve Shore'. 2019. Master's Thesis, Geophysical Sciences (Meteorology and Oceanography). Available from http://hdl.handle.net/10451/40479.

[28] Kirincich A. 'Remote Sensing of the Surface Wind Field over the Coastal Ocean via Direct Calibration of HF Radar Backscatter Power'. *Journal of Atmospheric and Oceanic Technology*. 2016; **33**:1377-1392.

[29] Barrick D.E., Peake W. H. 'A review of scattering from surfaces with different roughness scales'. *Radio Science.* 1968; **3**:865-868.

[30] Barrick D.E. 'Remote sensing of sea state by radar'. Chapter 12 In *Remote Sensing of the Troposphere*, V.E. Derr (Ed.), U.S. Government Printing Office, Washington, DC. 1972.

[31] Wait J.R. 'Theory of HF Ground Wave Backscatter from Sea Waves'. *J. Geophys. Res.* 1966; **71**(20):4839-4842.

[32] Saviano S., Kalampokis A., Zambianchi E., Uttieri M. 'A year-long assessment of wave measurements retrieved from an HF radar network in the Gulf of Naples (Tyrrhenian Sea, Western Mediterranean Sea)', *Journal of Operational Oceanography.* 2019; **12**(1):1-15.

[33] Shay L.K., Cook T.M., Peters H., Mariano A.J., Weisberg R.H., An P.E., Soloviev, A., Luther, M. 'Very High Frequency radar mapping of surface currents'. *IEEE Journal of Oceanic Engineering*. 2002; **27**(2):155-169.

[34] Martinez-Pedraja J., Shay L.K., Haus B.K., Whelan C. 'Interoperability of SeaSondes and Wellen Radars in Mapping Radial Surface Currents'. *Journal of Atmospheric and Oceanic Technology*. 2013; **30**:2662-2675.

[35] Nadai A., Kuroiwa H., Mizutori M., Sakai S. 'Measurement of ocean surface currents by the CRL HF ocean surface radar of FMCW type. Part 2. Current Vector'. *Journal of Oceanography*. 1999; **55**:13-30.

[36] Gurgel K.-W., Antonischki G., Essen H., Schlick T. 'Wellen Radar (WERA): A new ground wave HF radar for remote sensing'. *Coastal Engineering*. 1999a; **37**:219-234.

[37] Gurgel K.-W., Essen H.-H., Kingsley S.P. 'High-Frequency Radars: physical limitations and recent developments'. *Coastal Engineering*. 1999a; **37**:201-218.

[38] Schmidt R., 'Multiple emitter location and signal parameter estimation'. *IEEE Trans. Antennas. Propag.* 1986; **34**:276-280.

[39] Laws K.E., Fernandez D.M, Paduan J.D. 'Simulation based evaluations of HF radar ocean current algorithms'. *IEEE Journal of Oceanic Engineering*. 2000; **25**:481-491, doi:10.1109/48.895355.

[40] Barrick D.E., Lipa B. J. 'Evolution of bearing determination in HF current mapping radars'. Oceanography. 1997; **12**(2):72-75, doi:10.5670/oceanog.1997.27.

[41] de Paolo T., Terrill E. 'Skill assessment of resolving ocean surface current structure using compact-antenna-style HF radar and the MUSIC direction-finding algorithm'. *J. Atmos. Oceanic Technol.*, 2007; **24**:1277-1300, doi:10.1175/JTECH2040.1.

[42] Huang W., Gill E.W. HF Surface Wave radar. *Wiley Encyclopedia of Electrical and Electronics Engineering*. February 2019, pp. 1-11.

[43] Emery B., Washburn L. 'Uncertainty estimates for SeaSonde HF radar ocean current observations'. *Journal of Atmospheric and Oceanic Technology*. 2019; **36**(2):231-247, doi: 10.1175/JTECH-D-18-0104.1.

[44] Merz C.R., Liu Y., Gurgel K.-W., Petersen L., Weisberg R.H., 2015: Effect of Radio Frequency Interference (RFI) Noise Energy on WERA Performance Using the 'Listen Before Talk' Adaptive Noise Procedure on the West Florida Shelf. *Coastal Ocean Observing Systems: Advances and Syntheses*. Elsevier, doi:10.1016/B978-0-12-802022-7.00013-4.

[45] Chapman R.D., Shay L.K., Graber H.C., Edson J.B., Karachintsev A., Trump C.L., Ross D.B. 'On the accuracy of HF radar surface current measurements: Intercomparisions with ship-based sensors'. *Journal of Geophysical Research*. 1997; **102**(C8):18,737-18,748.

[46] Essen H-H., Gurgel K-W. 'On the accuracy of current measurements by means of HF radar'. *IEEE Journal of Oceanic Engineering*. 2000; **25**(4):472-480.

[47] Tiuri M.E., Sihvola A.H., Nyfors E.G., Hallikaiken M.T. 'The Complex Dielectric Constant of Snow at Microwave Frequencies'. *IEEE Journal of Oceanic Engineering*. 1984; **OE-9** (5):377-382.

[48] Rec. ITU-R P.453-9. 'The radio refractive index: its formula and refractivity data'. *International Télécommunication Union*. 2003.

[49] Tamosiunaite M., Tamosiunas S., Zilinskas M., Tamosiuniene M. 'Atmospheric Attenuation due to Humidity'. *IntechOpen*. 2011, doi: 10.5772/21430.

[50] Maresca S., Braca P., Grasso R., Horstmann J. 'The impact of sea state on HF surface-wave radar ship detection and tracking performances'. *Conference: Proc. of the OCEANS'15 MTS/IEEE Conference, Genova, 2015*, doi: 10.1109/OCEANS-Genova.2015.7271676.

[51] Liu Y., Weisberg R.H., Merz C.R., Lichtenwalner S., Kirkpatrick G.J. 'HF radar Performance in a low-energy environment: CODAR SeaSonde experience on the West Florida Shelf'. *J. Atmos. Oceanic Technol.*, 2010; **27**:1689–1710, doi:10.1175/2010JTECHO720.1.

[52] Liu Y., Weisberg R.H., Merz C.R. 'Assessment of CODAR SeaSonde and WERA HF Radars in Mapping Surface Currents on the West Florida Shelf'. *J. Atmos. Oceanic Technol.*, 2014; **31**:1363–1382, doi:10.1175/JTECH-D-13-00107.1.

[53] Merz C.R., Weisberg R.H., Liu Y. 'Evolution of the USF/CMS CODAR and WERA HF Radar Network'. *Oceans'12 MTS/IEEE Conference proceedings - Xplore*, Hampton Roads, VA, 2012; doi:10.1109/OCEANS.2012.6404947.

[54] Merz C.R. 'An Overview of the Coastal Ocean Monitoring and Prediction System (COMPS)'. *Oceans'01 MTS/IEEE Conference proceedings - IEEE Xplore,* Honolulu, HI*,* 2001, **2**: 1183-1187, doi:10.1109/OCEANS.2001.

[55] Liu Y., Merz C.R., Weisberg R.H., O'Loughlin B.K., Subramanian V. 'Data return aspects of CODAR and WERA high frequency radars in mapping currents' in Venkatesan et al. (eds.). *Observing the Oceans in Real Time*. Berlin: Springer; 2017. pp. 227-241, doi: 10.1007/978-3-319-66493-4_11.

[56] Gurgel K-W., Barbin Y., Schlick T. 'Radio Frequency Interference Suppression Techniques in FMCW Modulated HF Radars'. *OCEANS 2007 - Europe*, Aberdeen, UK, 2007, pp. 1-4, doi: 10.1109/OCEANSE.2007.4302289.

[57] Cosoli S. 'Implementation of the Listen-Before-Talk Mode for SeaSonde High-Frequency Ocean Radars'. *Journal of Marine Science and Engineering*. 2020; **8**(57):1-13, doi:10.3390/jmse8010057.